# Wireless Power Transfer With Concurrent 200-kHz and 6.78-MHz Operation in a Single-Transmitter Device

Dukju Ahn and Patrick P. Mercier, *Member, IEEE*

***Abstract*—This paper proposes a wireless power transfer (WPT) transmitter that can concurrently operate at 200 kHz and 6.78 MHz in order to simultaneously power two receivers operating with different frequency standards. Unlike a dual-resonant single-coil design, the use of two separate coils decouples the design for one frequency from the other, enabling independent selection of inductance and *Q*-factor to simultaneously maximize efficiency at both frequencies. The two coils then support separate coil drivers, enabling concurrent multistandard operation. Dual-band operation is achieved in the same area as an equivalent single-band design by placing a low-frequency coil within the geometry of a high-frequency coil, where the outer diameter of inner coil is sacrificed only by 1.2 cm in a 12.5 $\times$ 8.9-cm$^2$ design. Circuit analysis is presented to identify the eddy current between the two Tx coils and its associated loss, after which an eddy-current filter design is proposed. To validate the proposed design, a dual-mode transmitter, along with two receivers designed at 6.78 MHz and 200 kHz, respectively, have been fabricated. At 25-mm separation, the system is able to simultaneously deliver 9 and 7.4 W with efficiencies of 78% and 70.6% at 6.78 MHz and 200 kHz, respectively.**

***Index Terms*—Dual band, inductive power transfer, multistandard, resonant power transfer, wireless charging, wireless power.**

## I. Introduction

WIRELESS power transfer via resonant or nonresonant near-field magnetics is now accepted as a viable method to power many kinds of devices, including portable consumer electronics [1]–[4], electric vehicles [5], [6], and biomedical implants [7]–[9]. Given the convenience of charging mobile devices, such as smartwatches, smartphones, and laptops, wirelessly, there has been a much recent activity from industry to incorporate such technology into commercial products. Industry leaders have, thus, proposed wireless powering standards to ensure compatibility amongst differing products. However, there are currently three incompatible standards in use today that are managed by three separate organizations: the Alliance for Wireless Power (A4WP), the Wireless Power Consortium (WPC), and the Power Matters Alliance (PMA) [10]–[12].

Unfortunately, the operating frequency of each standard differs. For example, the A4WP standard [10] proposes to use a 6.78 MHz $\pm$ 15 kHz carrier frequency, while WPC [11] and PMA [12] use frequency ranges of 110–205 and 110–300 kHz, respectively. One advantage of wireless charging was conceived as the ability to simultaneously charge multiple receivers using a single transmitter, because family members in a house typically have multiple phones and laptops from different manufacturers. However, with different frequency standards for each receiver device, a single power transmitter cannot conventionally charge incompatible receivers simultaneously. Thus, there is a need to develop a single transmitter which can accommodate multiple receivers operating with different standards, and therefore, at different frequencies.

Although recent work has aimed to transfer power and data at separate frequencies, in some cases using multiples coils, such techniques have not been applied to multistandard wireless charging. The study in [13], for example, proposed a dual-frequency wireless power/ wireless data system for implantable electronics. The two Tx coils, one for power and another for data, are placed orthogonal to each other in the transmitter in order to prevent interference between the two coils. Although this was effective for power and data transmission to one receiver, this cannot be applied to a multireceiver use-case, because the receiver would also need to be equipped with orthogonal coils, which is not feasible in most portable devices that have thin, planar geometries. The study in [14] proposed a multifrequency inductive power transfer system, which amplified both the fundamental and the third harmonic generated by a full-bridge inverter in order to transfer power to a receiver at both frequencies. This study was, however, intended only for single-receiver operation, and cannot operate at both 200 kHz and 6.78 MHz.

On the other hand, the studies in [15] and [16] employed a single resonator with lumped impedance matching to enable wireless power transfer at two distinct frequencies. Specifically, [15] operated at 6.78 and 13.56 MHz, while [16] operated at 11 and 36 MHz. In these cases, the proposed single-coil approach has the advantage of less crosstalk over a two-coil solution. However, it is generally difficult to achieve high efficiency using a single coil, especially if the two frequencies differ significantly from each other. For example, the A4WP standard operates at 6.78 MHz, which is 33 times higher than the 200 kHz for WPC/PMA. As will be discussed in Section II, the required value of Tx inductance, and therefore, the coil size and number

Manuscript received March 23, 2015; revised June 12, 2015 and July 25, 2015; accepted September 15, 2015. Date of publication September 18, 2015; date of current version January 28, 2016. This work was supported by the Technology Development Program for Commercializing System Semiconductor funded by the Ministry of Trade, Industry, and Energy, Korea, under Grant 10041126 with title as International Collaborative R&D Project for System Semiconductor. Recommended for publication by Associate Editor C. Tse.

D. Ahn is with Incheon National University, Incheon 22012, Korea (e-mail: adjj22@gmail.com).

P. P. Mercier is with the University of Californai at San Diego, La Jolla, CA 92093 USA (e-mail: pmercier@ucsd.edu).

Color versions of one or more of the figures in this paper are available online at http://ieeexplore.ieee.org.

Digital Object Identifier 10.1109/TPEL.2015.2480122

of turns, for efficient power delivery varies significantly with operating frequency. Thus, a coil designed for 6.78 MHz will operate with degraded efficiency at 200 kHz. On the receiver side, the study in [3] proposed a dual-band receiver coil which was tuned for operation at both 100 kHz and 6.78 MHz. The receiver can be powered by any one of the three wireless power standards. However, receiver coils often have more strict size constraints than the transmitter, limiting achievable efficiency. For example, the 100-kHz coil in [3] is placed inside the 6.78-MHz coil with a gap between them, limiting the outer diameter of the 100-kHz coil, which thereby limits the coupling with the transmitter. On the other hand, implementing the dual-band capability into a transmitter, which has more generous volume than the receiver, would allow a more compact receiver with tighter coupling for higher overall efficiency.

In this paper, we propose to use two separate Tx coils which can be individually designed for each frequency: 200 kHz and 6.78 MHz. This enables concurrent dual-frequency operation with high efficiency. To minimize the increase in coil volume, the 200 kHz coil is embedded within the geometry of the 6.78 MHz coil. The receiver design is not altered by the concurrent operation, and thus, existing designs can still operate correctly with the proposed transmitter. To understand the loss components and trade-offs, exact circuit analysis for the system is presented, and a corresponding efficiency-boosting filter is designed and fabricated. It is demonstrated that the efficiency degradation due to the multifrequency support is in between 1.3% and 4.2% for various power levels.

This paper is organized as follows: Section II describes the challenges of using a single coil or a coil with adjustable inductance, specifically for the 200-kHz and 6.78-MHz frequency bands, Section III describes the proposed multifrequency transmitter and its analysis, Section IV presents implementation details, while Section V discusses measurement results. Finally, conclusions are drawn in Section VI.

## II. Challenges of Dual-Band Operation

To understand the challenges of dual-band operation, this section will first outline a circuit model for wireless power transfer, then discuss the parasitic effects of adopting a multiband strategy. The presented circuit analysis is based on the well-used general circuit model of a wireless power transfer system shown in Fig. 1. In this circuit, the effect of coupling between the Tx and Rx is abstracted as a reflected resistance $R_{\rm refl}$ [20]

$$\begin{aligned} R_{\rm refl} &= k^2\omega L_{\rm TX}\omega L_{\rm RX}/(R_L + R_{\rm RXparasitic}) \\ &= k^2\omega L_{\rm TX}\omega L_{\rm RX}/R_{\rm RX} \end{aligned} \tag{1}$$

where $L_{\rm TX}$ is the inductance of the transmitting coil $L_{\rm RX}$ is the inductance of the receiving coil $R_L$ is the receiver load resistance, $R_{\rm RXparasitic}$ is the parasitic resistances in receiver, $R_{\rm RX} = R_L + R_{\rm RXparasitic}$, and $k$ is the coupling coefficient between $L_{\rm TX}$ and $L_{\rm RX}$. The $R_{\rm refl}$ resistance is connected in series with the Tx coil $L_{\rm TX}$. The Tx inverter (or power amplifier), which is modeled as a voltage source $V_S$, is loaded by the reflected resistance $R_{\rm refl}$ and some parasitic resistance $R_{\rm TXparasitic}$. Note that capacitive tuning on the transmitter side can be incorporated for resonant operation, but is not shown here for simplicity. For high efficiency and high output power, $R_{\rm TXparasitic}$ should be designed to be as small as possible, while $R_{\rm refl}$ should be designed as a compromise between maximum power transfer (when matched to $R_{\rm TXparasitic}$), and maximum efficiency (when $R_{\rm refl} \gg R_{\rm TXparasitic}$) [17], [18], [20]. Since the power dissipated at $R_{\rm refl}$ is equivalent to the power transferred to receiver, efficiency can be calculated as

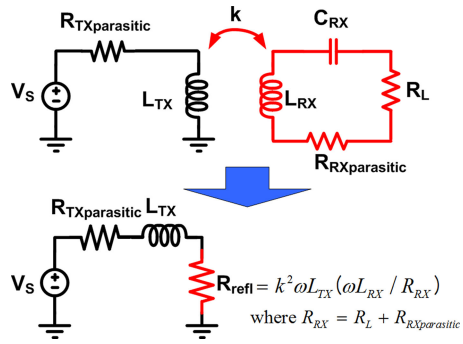


Fig. 1. Circuit model of basic wireless power-transfer system. The effect of receiver is abstracted as a reflected resistance $R_{\rm refl}$. The $R_{\rm refl}$ should be in appropriate range for the efficient operation of a Tx inverter.

$$\begin{aligned} \eta &= \frac{R_{\rm refl}}{R_{\rm TXparasitic} + R_{\rm refl}} \frac{R_L}{R_L + R_{\rm RXparasitic}} \\ &= \frac{k^2(\omega L_{\rm TX}/R_{\rm TXparasitic})(\omega L_{\rm RX}/R_{\rm RX})}{1 + k^2(\omega L_{\rm TX}/R_{\rm TXparasitic})(\omega L_{\rm RX}/R_{\rm RX})} \\ &\quad \times \frac{R_L}{R_L + R_{\rm RXparasitic}}. \end{aligned} \tag{2}$$

This implies that the efficiency can be high despite the low coupling $k$ between the Tx and Rx, so long that the resistances in the Tx and Rx coils are low compared to their reactive impedances. In other words, $(\omega L_{\rm TX}/R_{\rm TXparasitic})$ and $(\omega L_{\rm RX}/R_{\rm RX})$ compensate for the low coupling coefficient.

Since $k$ and receiver parameters $\omega L_{\rm RX}/(R_{\rm RXparasitic} + R_L)$ are roughly constant across frequency in practical designs, the reflected resistance is directly proportional to $\omega L_{\rm TX}$. This implies that a different value of $L_{\rm TX}$ is required for each operational frequency $\omega$ to ensure appropriate reflected resistance. For example, an inductance value of 1.2 $\mu$H is ideal for operation at 6.78 MHz in this study, as a coupling coefficient of 0.1 and a receiver quality factor $Q_{\rm RX}$ of 10, results in a reflected resistance is 5.1 $\Omega$, which is considerably higher than an $R_{\rm TXparasitic}$ of 0.5 $\Omega$ (comprising the parasitic resistance of the power MOSFET, transmitter coil, and PCB pattern traces). This setup results in a Tx efficiency of $5.1/(5.1 + 0.5) = 91\%$. However, for 200-kHz operation with the same $L_{\rm TX}$, $Q_{\rm RX}$, and $k$, the reflected resistance is only 0.15 $\Omega$, which is now comparable to the parasitic resistances. Assuming these parasitics are optimistically scaled to 0.1 $\Omega$ at 200 kHz, the Tx efficiency would be no greater than $0.15/(0.15 + 0.1) = 60\%$. As a result, it is important to design the Tx inductance $L_{\rm TX}$ to the appropriate value for each operational frequency. For this reason, a single Tx coil, even if coupled with an ideal dual-band resonant matching network, which in theory can enable concurrent operation, has difficulty achieving high efficiency, especially as the separation

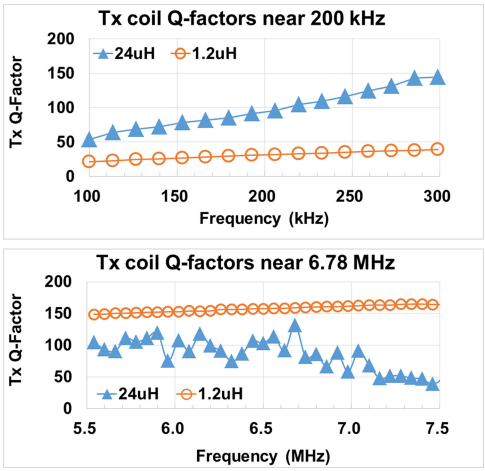


Fig. 2. Measured Tx coil Q-factors at two different frequency bands. The high-inductance coil is suitable for low-frequency operation, whereas the low-inductance coil is suitable for high-frequency operation.

between the two frequencies increase. For example, to increase the reflected impedance at 200 kHz, an $L_{\mathrm{TX}}$ of 24 $\mu$H would be ideal in this study, as it would produce several ohms of reflected resistance for increased efficiency and sufficient output power. While further increases to the inductance value could be made in both the 6.78-MHz and 200-kHz transmitters to increase the efficiency, the larger associated reflected resistance would serve to decrease the achievable transmitted power which is not necessarily desirable.

The $Q$-factor of a given Tx coil is also affected by the operational frequency. As shown in Fig. 2, the $Q$-factor of smaller inductors is generally maximized at higher frequencies (6.78 MHz), whereas that of larger inductors tends to be maximized at lower frequency (200 kHz). Since it can be shown that the efficiency and power transfer capabilities of wireless power transfer links both increase with $Q$ of the constituent coils [18], and given the analysis presented in the preceding paragraph, it is desirable to operate high-frequency coils with smaller Tx inductance and low-frequency coils with larger Tx inductance.

Unfortunately, it is difficult to design coils with variable inductance or design matching networks with two resonant frequencies, especially when one of the desired operating frequencies is 30 times higher than the other. For example, it should be possible in theory to use a switch inserted into a tap point in the inductor to dynamically select the appropriate amount of the desired inductance for time-sequenced dual-band operation, as was presented in [18]. However, unlike [18], which operated at a single frequency, the switch parasitics in multifrequency operation limit the effectiveness of this technique. For example, Fig. 3 illustrates a Tx schematic which has a switch to disconnect the 200-kHz Tx coil. Unfortunately, the typical parasitic capacitance of a high-power MOSFET is on the order of $\sim$100 pF, which easily (and unintentionally) resonates with the lower frequency coil. To illustrate, a 19-$\mu$H Tx coil designed for operation at 200 kHz resonates at 3.7 MHz with the 100-pF parasitic capacitor. Thus, at 6.78 MHz, the reactive impedance of the 100-pF capacitor is much lower than that of the 19-$\mu$H

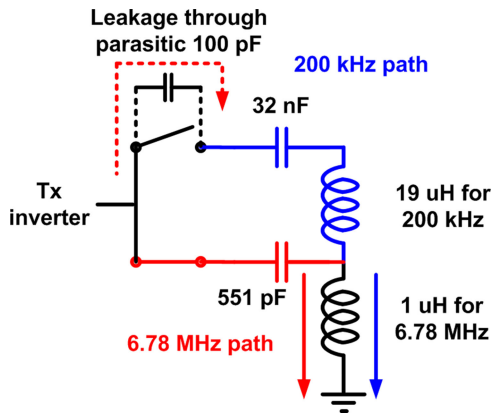


Fig. 3. Tx which has a switch to disconnect the 200-kHz Tx coil, when 6.78 MHz is in operation. Unfortunately, the 200-kHz coil is not easily disconnected due to the parasitic capacitance of switch.

inductance, and therefore, effectively shorts the 19-$\mu$H Tx coil into the 6.78-MHz power path. Once the 19-$\mu$H 200-kHz Tx coil is shorted to the 6.78-MHz path, it behaves as an eddy-current loop for the 6.78-MHz transmitter, since the two Tx coils are closely packed within a single Tx device. SPICE-level coil simulations indicate that the efficiency is degraded from 89.2% to 57%, when a parasitic capacitance of 100 pF is introduced.

Another drawback of Tx coil selection using a switch is that only one frequency can be activated at a time. Thus, although the Tx charging pad area is often wide enough to accommodate multiple receivers, only one receiver can be charged if the frequencies of each receiver are different. For these reasons, switch-tuned dual-band operation is not considered further.

## III. Proposed Concurrent Dual-Band Wireless Power Transmitter

To enable concurrent dual-band frequency operation with high efficiency, the proposed transmitter is implemented with two separate coils $L_{6.78M}$ and $L_{200k}$, appropriately sized for maximal efficiency at 6.78 MHz and 200 kHz, respectively. As illustrated in Fig. 4(a), each coil features shunting and/or blocking filters to reduce coupled losses. Here, an auxiliary resonant tank $L_F - C_F$ is added in series with the 200-kHz stage, and is tuned to a resonant frequency of 6.78 MHz. This tank then acts as a filter whose impedance is high at 6.78 MHz, which helps to minimize both the undesired crosstalk from the 6.78-MHz power carrier to 200 kHz-power transistors, and the eddy current losses of the 6.78-MHz transmitter through the 200-kHz path. The $C_{200k}$ is then tuned to compensate for the sum of $L_{200k}$ and $L_F$. Similarly, capacitors $C_{6.78M}$, which are nominally required in the 6.78-MHz path for resonant operation, act as a high-impedance filter to the 200-kHz inverter, minimizing losses during 200-kHz operation. The following subsections present analytical expressions to determine the parameters of the circuits in Fig. 4.

### A. 6.78-MHz Operation Mode

The low impedance of $C_{\mathrm{oss}}$ and $C_{\mathrm{shunt}}$ in the 200-kHz output network behaves as an eddy current loop for 6.78-MHz

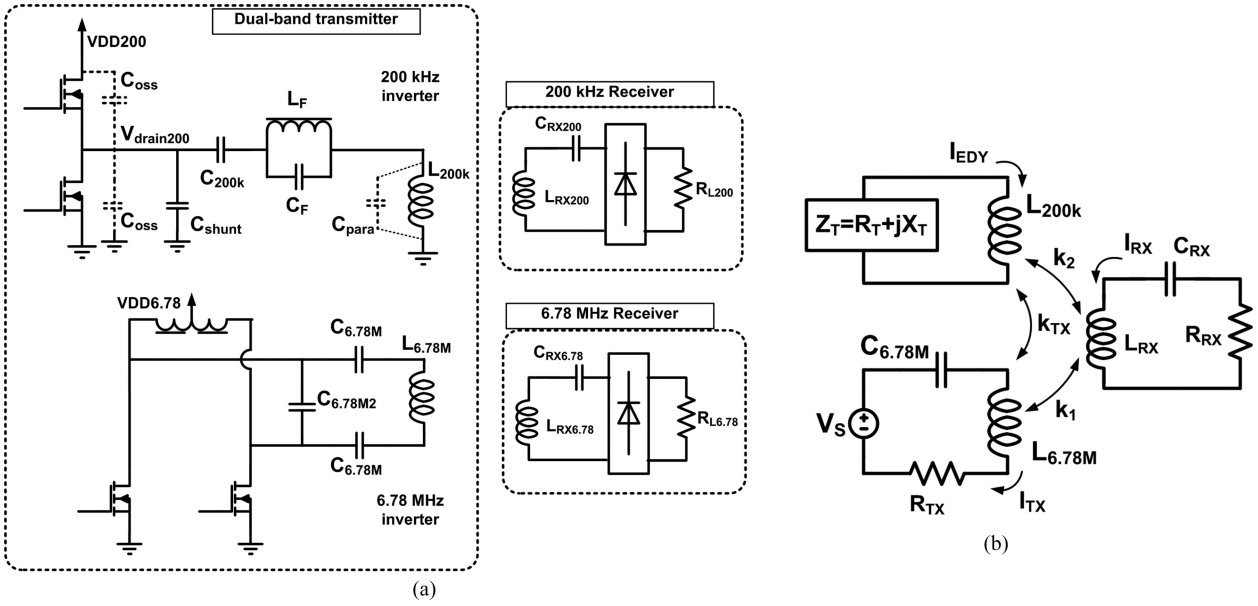


Fig. 4. (a) Proposed dual-band wireless power transmitter which can simultaneously power two receivers of different frequency standard. (b) Circuit model for coil analysis.

carrier, if the $L_F - C_F$ filter is not used. The required impedance value of the $L_F - C_F$ tank can be determined by analyzing the circuit of Fig. 4(b). Impedance $\mathbf{Z_T}$ shown in Fig. 4(b) is the total impedance along the eddy current loop, which consists of $L_F||C_F$, $C_{200k}$, $C_{\rm oss} + C_{\rm shunt}$, $C_{\rm para}$, and the parasitic resistance of $L_{200k}$. Fig. 4(b) can be characterized by the following Kirchoff's voltage law expressions:

$$\begin{aligned}
&\left(j\omega L_{6.78} - j\frac{1}{\omega C_{6.78}} + R_{\rm TX}\right)\mathbf{I_{TX}} + jk_1\omega\sqrt{L_{6.78}L_{\rm RX}}\mathbf{I_{RX}} \\
&+jk_{\rm TX}\omega\sqrt{L_{6.78}L_{200}}\mathbf{I_{EDY}} = \mathbf{V_S} \\
&jk_1\omega\sqrt{L_{6.78}L_{\rm RX}}\mathbf{I_{TX}} + \left(j\omega L_{\rm RX} - j\frac{1}{\omega C_{\rm RX}} + R_{\rm RX}\right)\mathbf{I_{RX}} \\
&+jk_2\omega\sqrt{L_{200}L_{\rm RX}}\mathbf{I_{EDY}} = 0 \\
&jk_{\rm TX}\omega\sqrt{L_{6.78}L_{200}}\mathbf{I_{TX}} + jk_2\omega\sqrt{L_{\rm RX}L_{200}}\mathbf{I_{RX}} \\
&+\left(j\omega L_{200} + \mathbf{Z_T}\right)\mathbf{I_{EDY}} = 0
\end{aligned} \tag{3}$$

where $\omega$ is the 6.78-MHz operating frequency, $k_{\rm TX}$, $k_1$, and $k_2$ are the coupling coefficients between the coils, and $\mathbf{I_{TX}}$, $\mathbf{I_{RX}}$, and $\mathbf{I_{EDY}}$ are the coil current phasors. Simplifying (3) at resonance yields

$$\begin{aligned}
&\left(\frac{R_{\rm TX}}{j\omega L_{6.78}}\right)\mathbf{I_{TX}} + k_1\sqrt{\frac{L_{\rm RX}}{L_{6.78}}}\mathbf{I_{RX}} \\
&+k_{\rm TX}\sqrt{\frac{L_{200}}{L_{6.78}}}\mathbf{I_{EDY}} = \frac{\mathbf{V_S}}{j\omega L_{6.78}} \\
&k_1\sqrt{\frac{L_{6.78}}{L_{\rm RX}}}\mathbf{I_{TX}} + \frac{1}{jQ_{\rm RX}}\mathbf{I_{RX}} + k_2\sqrt{\frac{L_{200}}{L_{\rm RX}}}\mathbf{I_{EDY}} = 0 \\
&k_{\rm TX}\sqrt{\frac{L_{6.78}}{L_{200}}}\mathbf{I_{TX}} + k_2\sqrt{\frac{L_{\rm RX}}{L_{200}}}\mathbf{I_{RX}} \\
&+\left(1 + \frac{\mathbf{Z_T}}{j\omega L_{200}}\right)\mathbf{I_{EDY}} = 0
\end{aligned} \tag{4}$$

where $Q_{\rm RX} = \omega L_{\rm RX}/R_{\rm RX}$. By solving (4), we can obtain $\mathbf{I_{TX}}/\mathbf{I_{RX}}$, which indicates how much Tx driving current is required to deliver a given amount of current across receiver load

$$\frac{\mathbf{I_{TX}}}{\mathbf{I_{RX}}} = -\frac{\frac{\mathbf{Z_T}}{\omega L_{200}} + k_2^2 Q_{\rm RX} + j}{k_1 Q_{\rm RX}\left(\frac{k_2}{k_1}k_{\rm TX} - 1 + j\frac{\mathbf{Z_T}}{\omega L_{200}}\right)}\sqrt{\frac{L_{\rm RX}}{L_{\rm TX}}}. \tag{5}$$

Equation (5) indicates that the required driving current depends on $\mathbf{Z_T}$.

*1) Operation without $L_F - C_F$ Filter:* Now suppose that the $L_F - C_F$ filter is not used. Then, $\mathbf{Z_T}$ is the sum of impedances of $C_{200k}, C_{\rm oss} + C_{\rm shunt}$, and the parasitic resistance of $L_{200k}$. Capacitance $C_{\rm oss}$, which is the parasitic capacitance of the MOSFET switches, is typically higher than 100 pF. In addition, $C_{\rm shunt}$ is needed to suppress the high voltage interference from 6.78 MHz. Assuming the minimum value of $C_{\rm oss}$ is 100 pF, its impedance at 6.78 MHz is $-j235\ \Omega$, which is one fifth of the impedance of $\omega L_{200k} = j1080W$. The parasitic resistance of $L_{200k}$, which is the real part of $\mathbf{Z_T}$, is typically a few ohms. That means the real and imaginary parts of impedance $\mathbf{Z_T}$ are small compared to $\omega L_{200k}$, i.e., $|\mathbf{Z_T}| \ll wL_{200k}$. Thus, (5) becomes

$$\frac{\mathbf{I_{TX}}}{\mathbf{I_{RX}}} \cong -\frac{k_2^2 Q_{\rm RX} + j1}{k_1 Q_{\rm RX}\left(\frac{k_2}{k_1}k_{\rm TX} - 1\right)}\sqrt{\frac{L_{\rm RX}}{L_{\rm TX}}}. \tag{6}$$

This implies that the required Tx driving current is increased by a factor of $1/(1-(k_2/k_1)k_{\rm TX})$, if the $L_F - C_F$ filter is not used. This matches intuition, since a significant portion of the magnetic field from the driving current is cancelled by the magnetic fields stemming from the resulting eddy currents. A high level of Tx driving current for a given received power implies

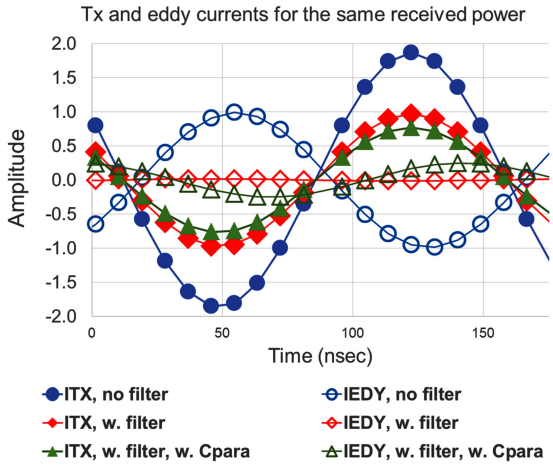


Fig. 5. Simulated current waveforms with and without the $L_F - C_F$ filter. Without the high-Z filter, higher Tx driving current is required due to severe eddy currents that cancel the magnetic field. The eddy currents are scaled by a factor of $\sqrt{L_{200}/L_{\rm TX}}$.

higher ohmic losses in the Tx coil and MOSFETs, which reduces efficiency. A thicker coil would then be required to withstand high resonant current and heat generation. Moreover, constituent semiconductor switches and passive components would need to withstand higher voltage and current ratings, which increase fabrication cost and often further increase parasitics. Since the two Tx coils $L_{6.78M}$ and $L_{200k}$ are closely placed within a single transmitter device, the $k_{\rm TX}$ value can be as high as 0.4–0.6, meaning that the driving current should be approximately doubled to transfer the same power.

The eddy current can be directly found by solving $\mathbf{I_{EDY}}/\mathbf{I_{TX}}$ from (4)

$$\frac{\mathbf{I_{EDY}}}{\mathbf{I_{TX}}} = -\frac{k_1 k_2 Q_{\rm RX} + j k_{\rm TX}}{\frac{\mathbf{Z_T}}{\omega L_{200}} + k_2^2 Q_{\rm RX} + j1}\sqrt{\frac{L_{\rm TX}}{L_{200}}}. \tag{7}$$

In (7), if $\mathbf{Z_T}$ is small, the $jk_{\rm TX}$ and $j1$ become the dominant terms and the phase of $\mathbf{I_{EDY}}$ with respect to $\mathbf{I_{TX}}$ is opposite.

*2) Operation with $L_F - C_F$ Filter:* However, if the $L_F - C_F$ filter is used, then $\mathbf{Z_T} \gg wL_{200}$ is satisfied and Equation (5) simplifies to

$$\frac{\mathbf{I_{TX}}}{\mathbf{I_{RX}}} = j\frac{1}{k_1 Q_{\rm RX}}\sqrt{\frac{L_{\rm RX}}{L_{\rm TX}}}. \tag{8}$$

This is equivalent to the case, where there are no eddy current paths (i.e., see Equation (8) in [19]). Therefore, it is desirable to set the impedance $\mathbf{Z_T}$ to be high as compared to $\omega L_{200}$ in order to prevent eddy currents, and therefore, maintain a low Tx driving current. Doing so will prevent excessive ohmic losses at the Tx coil, while also limiting the otherwise necessary high voltage or current stress in the Tx devices.

To illustrate these findings, Fig. 5 shows simulated current waveforms across three separate conditions, all for equal amount of received power (set by adjusting the Tx driving current). The eddy currents are scaled by a factor of $\sqrt{L_{200}/L_{\rm TX}}$ to better visualize the contribution of the eddy current on the magnetic field cancellation with respect to the Tx driving current. The blue circle curves with the "no filter" label illustrate the case where the $L_F - C_F$ filter is not used and the eddy current flows through $L_{200k} - C_{200k} - C_{\rm shunt}$. It can be seen that the eddy current$I_{\rm EDY}$ is high and that the Tx driving current $I_{\rm TX}$ is twice the amplitude of the high impedance cases. On the other hand, the "w. filter" labels using red diamonds indicate that the Tx driving current is small and the eddy current is suppressed.

In practice, however, there exists a parasitic capacitance $C_{\rm para}$ within $L_{200k}$. For example, the measured parasitic capacitance of a 24-$\mu$H, 7 cm $\times$ 10.5 cm coil is 9.5 pF. The Tx currents, when this parasitic is incorporated into the simulation model, are shown as the yellow triangular curves in Fig. 5. Although the eddy current is slightly increased compared to the zero-parasitic case, this eddy current does not significantly degrade the efficiency. The notable change is that this small eddy current is now almost in-phase with the Tx driving current, thereby reinforcing the magnetic field generated from Tx driving current, not cancelling it. As a result, the required Tx driving current, $I_{\rm TX}$, with filter, with $C_{\rm para}$, is the lowest amongst all three presented simulations. Note that "no filter with $C_{\rm para}$" is essentially the same as "no filter without $C_{\rm para}$," because $C_{\rm para}$ is connected in parallel with $C_{\rm shunt}$ and $C_{\rm oss}$ if the $L_F - C_F$ filter is not used, and since $C_{\rm shunt}$ and $C_{\rm oss}$ is much larger than $C_{\rm para}$, the effect of $C_{\rm para}$ is negligible when $L_F - C_F$ is not used. For the example presented in Fig. 5, the simulated coil efficiencies of no filter, with filter, and with filter and $C_{\rm para}$ are 83.2%, 89.2%, and 88.6%, respectively. Note that while the inclusion of $C_{\rm para}$ helps to reduce the Tx driving current, it does slightly degrade efficiency, in this case by less than 1%.

The phase change of the eddy currents can be analyzed from (7) by setting $\mathbf{Z_T} = \mathbf{1}/(\mathbf{j}\omega\mathbf{C}_{\rm para})$ assuming that the $L_F - C_F$ impedance is sufficiently high

$$\frac{\mathbf{I_{EDY}}}{\mathbf{I_{TX}}} = -\frac{k_1 k_2 Q_{\rm RX} + j k_{\rm TX}}{k_2^2 Q_{\rm RX} + j\left(1 - \frac{\omega_{\rm self}^2}{\omega^2}\right)}\sqrt{\frac{L_{\rm TX}}{L_{200}}}. \tag{9}$$

Here, $\omega_{\rm self} = 1/\sqrt{L_{200}C_{\rm para}}$ is the self-resonant frequency of $L_{200k}$. If $\omega_{\rm self} > \omega$, $\mathbf{I_{EDY}}$ is close to being in-phase with $\mathbf{I_{TX}}$. The self-resonant frequency should not be lower than 6.78 MHz to prevent the field-cancelling eddy current.

*3) Efficiency Versus Filter Impedance:* Although the eddy current is significantly suppressed by the proposed high-impedance filter, the power loss across the eddy current path still needs to be investigated, since the real part of the impedance of the eddy current path is now high. To evaluate the contributions of each loss component, the overall resonator efficiency $\eta$ based on the derivation in [19] can be rewritten as

$$\begin{aligned}\eta &= \frac{R_{\rm RX}\left|\mathbf{I_{RX}}\right|^2}{R_{\rm TX}\left|\mathbf{I_{TX}}\right|^2 + R_{\rm RX}\left|\mathbf{I_{RX}}\right|^2 + {\rm Re}(\mathbf{Z_T})\left|\mathbf{I_{EDY}}\right|^2} \\ &= \frac{R_{\rm RX}}{R_{\rm TX}\left|\mathbf{I_{TX}}/\mathbf{I_{RX}}\right|^2 + R_{\rm RX} + {\rm Re}(\mathbf{Z_T})\left|\mathbf{I_{EDY}}/\mathbf{I_{RX}}\right|^2}\end{aligned} \tag{10}$$

where $R_{\rm TX}|\mathbf{I_{TX}}/\mathbf{I_{RX}}|^2$ and ${\rm Re}(\mathbf{Z_T})|\mathbf{I_{EDY}}/\mathbf{I_{RX}}|^2$ are the relative power loss at Tx coil and eddy current path, respectively, with respect to the power delivered to receiver. The $\mathbf{I_{EDY}}/\mathbf{I_{RX}}$

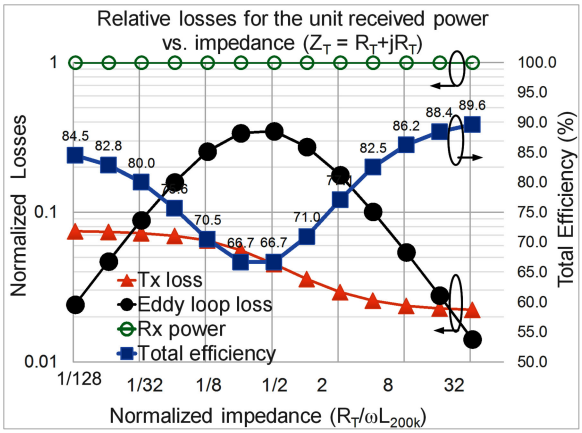


Fig. 6. Calculated losses for each coil and total coil efficiency, plotted with respect to $R_T$ (both real and imaginary part of $Z_T$ is set to $R_T$, because filters with high real part tend to have high imaginary part). The filter impedance should be high compared with $\omega L_{200k}$ to minimize both the eddy loop loss and Tx coil loss. With 11.2 $\mu$H and 47 pF, an $R_T/\omega L_{200k}$ value of 25 is obtained.

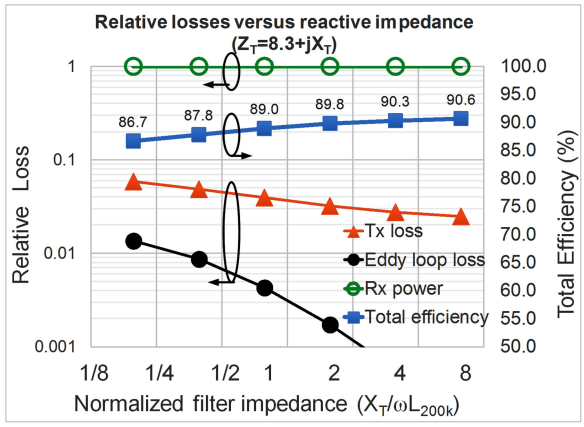


Fig. 7. Calculated losses, if the impedance $Z_T$ consists of mainly inductance. With 10-$\mu$H $L_F$, the $X_T/\omega L_{200k}$ value of only 0.47 is obtained. The eddy current is not completely suppressed and Tx loss is high.

can then be calculated as

$$\frac{\mathbf{I_{EDY}}}{\mathbf{I_{RX}}} = \frac{j(k_{\mathrm{TX}} - jk_1k_2Q_{\mathrm{RX}})}{k_1Q_{\mathrm{RX}}\left(\frac{k_2}{k_1}k_{\mathrm{TX}} - 1 + j\frac{\mathbf{Z_T}}{\omega L_{200}}\right)}\sqrt{\frac{L_{\mathrm{RX}}}{L_{200}}} \quad (11)$$

If the high-impedance filter is used (with $|\mathbf{Z_T}| \gg wL_{200}$), the relative power loss in the eddy current path $\mathrm{Re}(\mathbf{Z_T})$ $|\mathbf{I_{EDY}}/\mathbf{I_{RX}}|^2$ can be modeled as

$$\mathrm{Re}(\mathbf{Z_T})\left|\frac{\mathbf{I_{EDY}}}{\mathbf{I_{RX}}}\right|^2 \cong \mathrm{Re}(\mathbf{Z_T})\frac{k_{\mathrm{TX}}^2 + k_1^2k_2^2Q_{\mathrm{RX}}^2}{k_1^2Q_{\mathrm{RX}}^2\frac{|\mathbf{Z_T}|^2}{\omega^2L_{200}^2}}\frac{L_{\mathrm{RX}}}{L_{200}}. \quad (12)$$

In practice, $k_{\mathrm{TX}}^2$ is higher than $k_1^2k_2^2Q_{\mathrm{RX}}^2$ in (12). Therefore, it is desirable to reduce $k_{\mathrm{TX}}$ as much as possible to minimize power losses in the eddy current path. Section IV-A will discuss the coil design that addresses this concern in more detail.

Note that (12) also indicates that the magnitude of impedance $\mathbf{Z_T}$ should be large in order to reduce the power loss in eddy current loop, as was also discovered in the preceding section. Even if the impedance is dominated by the real part of $\mathbf{Z_T}$, Equation (12) predicts that the power loss is inversely proportional to the resistance, which nicely matches intuition since the eddy current is inversely proportional to the resistance, while the power loss is proportional to resistor and to square of eddy current. Note that this trend is valid only when $|\mathbf{Z_T}| \gg wL_{200}$. At very low filter impedances, a lower impedance yields higher efficiency because the eddy current does not dissipate ohmic power due to low parasitic resistance.

Fortunately, the employed $L_F - C_F$ filter can produce a high impedance near resonance. Measurement result of an implemented $L_F - C_F$ filter indicates that a 10-$\mu$H carbonyl core inductor and 47-pF capacitance produces 25874 + j23900 $\Omega$ at 6.78 MHz, which is more than 25 times larger than $\omega L_{200}$. The selection of the 11.2-$\mu$H value will be discussed in Section IV-B.

To illustrate the effectiveness of the proposed $L_F - C_F$ filter, Fig. 6 shows the calculated losses for each loss component using (5), (10), and (11), along with the achievable wireless power transfer efficiency based on measured parameters from an experiment setup. When $R_T$ is equivalent to the parasitic resistance of $L_{200k}$, which is 8.3 $\Omega$ in this example, the normalized impedance is $8.3/(\omega L_{200k}) - 1/128$. At this low impedance, the Tx coil losses are high because the Tx current is high for a given received power due to severe eddy currents. As $R_T$ is gradually increased, Tx coil losses are reduced. The eddy loop loss is very high when $R_T$ is approximately half of $\omega L_{200k}$. At this middle impedance point, the eddy current is not completely blocked while the real part of $\mathbf{Z_T}$, which dissipates power, is large. Hence, the filter impedance should not be near $\omega L_{200k}$. At high impedance, the eddy current is heavily suppressed and, therefore, both the Tx losses and eddy loop losses are minimized.

It is difficult to obtain the desired high impedance if $C_F$ is not used. For example, the measured impedances of the 11.2-$\mu$H $L_F$ with and without $C_F$ are 22538 + j25412 and 4.4 + j477 $\Omega$, respectively. The normalized impedance of j477 $\Omega$ with respect to $\omega L_{200k}$ is only 0.47. Fig. 7 illustrates the calculated losses, when the impedance $\mathbf{Z_T}$ mainly consists of inductance $L_F$ and an 8.3-$\Omega$ parasitic resistance from $L_{200k}$. At higher filter impedances, the eddy loop losses can be lowered and the total efficiency can be higher than the case of Fig. 6. However, it is not practical to implement such high impedance by only using $L_F$, because high $L_F$ degrades the efficiency in the 200-kHz mode, increasing the system volume and voltage stress across $C_{200k}$. When the normalized impedance of the pure inductor is 0.47 as in this case, the eddy current is not sufficiently blocked and the Tx coil loss is twice that of Fig. 6.

In summary, the 6.78-MHz operation requires an eddy current blocking filter in the 200-kHz output network to minimize losses, and the proposed $L_F - C_F$ can provide the requisite high impedance for efficient operation. Note that although the 200-kHz receiver is not present in the analysis of Section III-A, its presence causes little impact on 6.78-MHz mode efficiency. This is discussed in the Appendix.

### B. 200-kHz Operation Mode

When the 200-kHz power carrier flows through $L_{200k}$, eddy currents flow through the $L_{6.78M} - C_{6.78M} - C_{6.78M2}$ path.

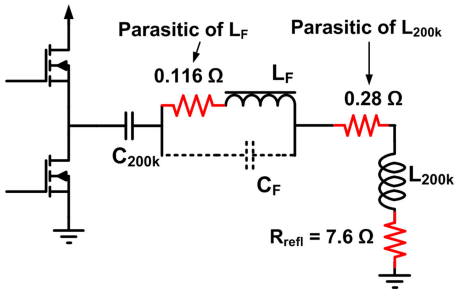


Fig. 8. Equivalent model at 200-kHz operation. The parasitic resistance of $L_F$ does not significantly degrade the 200-kHz mode efficiency because reflected resistance is larger.

However, this eddy current is small because $C_{6.78M}$, which is inherently needed to provide resonant operation and output matching, behaves as a high-impedance filter at 200 kHz. Moreover, the inductance of $L_{6.78M}$ is also small. Following the similar procedure as outlined by (5)–(8), and knowing that $\mathbf{Z_T} = 1/(j\omega' C_{6.78M}) = -j795\Omega \gg \omega' * L_{6.78M} = 1.5\Omega$, where $\omega'$ is $2\pi \times 200$ kHz, the 6.78 MHz path is seen as a nearly open-circuit network by the 200-kHz power carrier signal. Therefore, any additional filter beyond the inherent 6.78-MHz resonant tuning is not necessary for the 200-kHz operation mode.

Although the $L_F - C_F$ filter appears in series with the load, and thus, should slightly increase losses, in practice the additional losses are not significant. Fig. 8 illustrates the equivalent model of the 200-kHz transmitter when the filter is included. At low frequencies, the impedance of $C_F$ is very high and almost all current flows through $L_F$, which contributes a small parasitic resistance at 200 kHz. The measured inductance and parasitic resistance of $L_F$ are 9.6 $\mu$H and 0.116 Ω at 200 kHz, respectively. The 0.116-Ω parasitic resistance degrades the efficiency in the 200-kHz mode only by 1.3%, since the reflected resistance from the receiver to $L_{200k}$ is 7.6 Ω and the series loss of $L_{200k}$ is 0.28 Ω. The measured total system efficiency of 200-kHz mode with and without the $L_F - C_F$ filter are 70.2% and 71.5%, respectively.

## IV. Implementation

### A. Tx-Coil Design

The two Tx coils can be arranged in two different manners—coplanar or vertically stacked. The placement selection is a trade-off between 6.78-MHz efficiency, 200-kHz efficiency, and physical device size. Table I and Fig. 9 compare the two possible Tx structures. The 200-kHz Tx coil can be best coupled to its receiver if the 200-kHz Tx coil is vertically stacked over the 6.78-MHz coil. However, this lowers the efficiency at 6.78 MHz since this increases the coupling between the two Tx coils $k_{\mathrm{TX}}$ exacerbating eddy current losses. Moreover, the 6.78-MHz coil cannot be tightly coupled to its receiver, because the distance between the 6.78 MHz Tx and Rx is now increased. The vertical thickness of the overall Tx device becomes also bulky. On the other hand, the 6.78-MHz mode performs best if its Tx coil is placed outside of the 200-kHz Tx coil in a single plane. Here, the eddy current loss is minimized and the Tx-to-Rx coupling is maximal. However, the efficiency at 200 kHz is sacrificed due to the limited outer diameter of the 200-kHz Tx coil. In fact, the outer radius of the 200-kHz Tx coil is 6 mm smaller than that of the 6.78 MHz coil in this case. As a result, the efficiency at 200 kHz is degraded by 1.5% as shown in Table I, and the allowed lateral misalignment range of the 200-kHz mode is slightly narrower (by 6 mm) as will be shown in Section V.

The coplanar configuration can also be built in two different ways: inner 200 kHz–outer 6.78 MHz coils, or inner 6.78 MHz–outer 200 kHz coils. The former case is preferred, as the sacrificed outer radius of the 200-kHz coil is only 6 mm since the 6.78 MHz coil has a lower number of turns. Instead of a 6-mm sacrifice, placing the 6.78-MHz coil inside the 200-kHz coil would sacrifice the outer radius of the 6.78-MHz coil by 20 mm, which is not acceptable due to low efficiency as shown in Table I, and would further make the coupling between 6.78-MHz Tx and Rx too sensitive to lateral misalignment and vertical separation.

Based on this analysis, the fabricated Tx coils used in this work employ a coplanar design with the 200-kHz coil packed within the 6.78-MHz coil, as shown in Fig. 10. This enables the thinnest possible design, and as an added benefit, the current rating of the $L_F$ filter inductor can be relaxed, since the eddy current is the lowest in this configuration.

The 200-kHz and 6.78-MHz coils are built using 20-AWG and 16-AWG solid wires, respectively. The wire gauge of the 6.78-MHz coil can be thick because it requires only two turns and smaller volume. On the other hand, the wire gauge of the 200-kHz coil should be thinner, because it requires 13 turns and occupies large volume. Otherwise, a thicker wire with 13 turns would reduce the inner diameter, thereby degrading the inductance value and receiver coupling performance.

### B. $L_F - C_F$ Value Selection

The equivalent impedance of the $L_F - C_F$ resonant tank at $\omega_0 = 1/\sqrt{L_F C_F} = 2\pi \times 6.78\,\mathrm{MHz}$ can be found by looking at the input impedance of the parallel resonant *LC* tank, as given in (13)

$$\mathbf{Z_F} = (\omega_0 L_F)^2 / R_P - j1/(\omega_0 C_F) \tag{13}$$

where $R_P$ is the parasitic resistance of $L_F$. While a larger $L_F$ can achieve a higher impedance for superior performance in the 6.78-MHz mode, such a choice would degrade efficiency at 200 kHz, because the large inductance also increases the parasitic resistance in series with the 200-kHz Tx coil, as shown in Fig. 8. Fig. 11 shows this trade-off. The capacitor is selected such that resonance occurs with selected inductor value. The selected value of $L_F$ and $C_F$ is 11.2 $\mu$H and 47 pF, respectively. A toroid carbonyl core with a 3.3-cm outer diameter is used to wind $L_F$. The ac flux density inside the core is estimated as 26.6 G, which is ten times lower than the allowed limit. The measured impedance at 6.78 MHz is 25900 + $j$23900 Ω. As desired, the magnitude of this impedance is 35 times higher than $\omega L_{200k}$ at 6.78 MHz.

TABLE I
COMPARISON OF COPLANAR AND VERTICALLY-STACKED TXS

| Tx configurations | 6.78-MHz mode parameters | | | | | | 200-kHz mode parameters | |
|---|---|---|---|---|---|---|---|---|
| | $k_{\mathrm{TX}}$ † | $k_1$ † | $k_2$ † | Eddy loss per unit Rx power | Tx loss per unit Rx power | Efficiency | $k_2$ † | Efficiency |
| Coplanar, 6.78 MHz outer | 0.47 | 0.12 | 0.129 | 0.047 | 0.019 | 87.1% | 0.129 | 79.2% |
| Coplanar, 6.78 MHz inner | 0.39 | 0.071 | 0.142 | 0.068 | 0.043 | 83.6% | 0.142 | 80.7% |
| Vertically-stacked, 2 mm separation | 0.65 | 0.111 | 0.142 | 0.073 | 0.017 | 85.2% | 0.142 | 80.7% |
| Vertically-stacked, 5 mm separation | 0.54 | 0.099 | 0.142 | 0.068 | 0.022 | 85.2% | 0.142 | 80.7% |

† Coupling coefficients are extracted by HFSS full-wave electromagnetic simulation. Simulated S-parameter matrix is converted to Z-parameters, which contain self and mutual inductance, from which the coupling coefficient is extracted. The procedure is similar to Section V-A in [13].

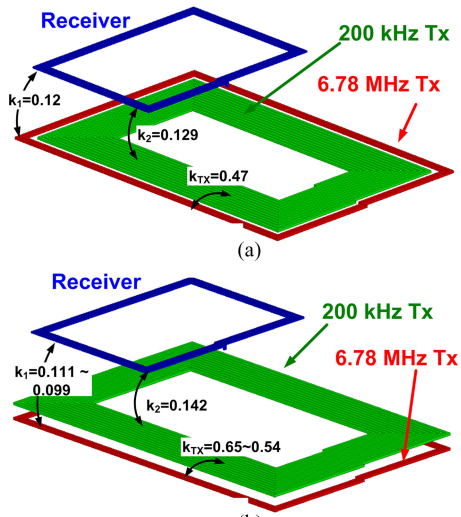


Fig. 9. Possible Tx configurations. (a) Coplanar. (b) Vertically-stacked.

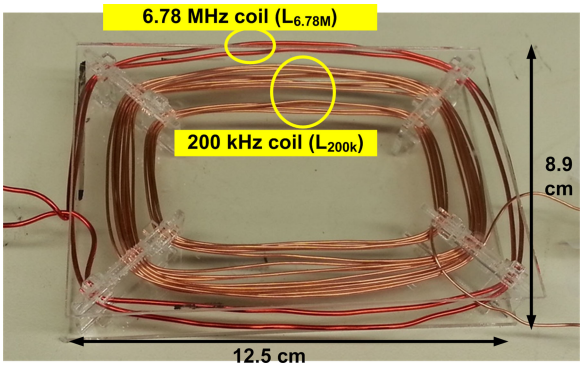


Fig. 10. Fabricated Tx coils: one coil for each operational frequency. Each coil can be designed for maximum efficiency for its own frequency, and enables concurrent operation. Because one coil is within another Tx coil, the overall size of coils is not increased.

### C. Power Converters

The 6.78-MHz path employs a current-switching Class-D inverter for the coil driver. This topology achieves a higher efficiency at high frequency, since the output parasitic capacitances of the MOSFETs can be absorbed by $C_{6.78M2}$. FDMC86106LZ MOSFET transistors are used due to their low parasitic capacitance and on-resistance. The input voltage to 6.78-MHz inverter is 12 V at full load. The 6.78-MHz receiver employs

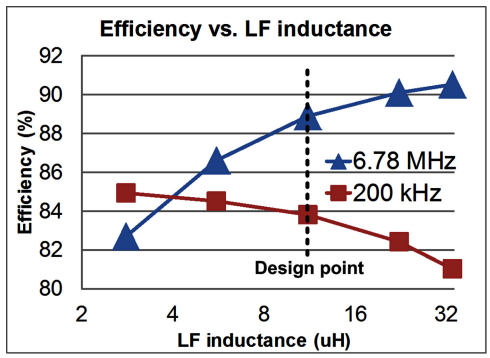


Fig. 11. Simulated efficiency versus $L_{\mathrm{F}}$ filter inductance. The selection of $L_{\mathrm{F}}$ value is a trade-off between 6.78 MHz and 200 kHz.

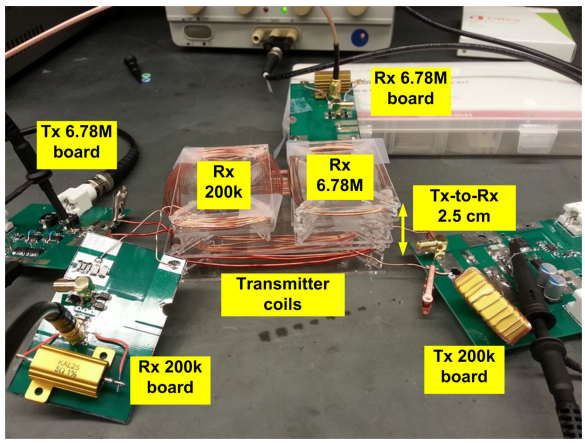


Fig. 12. Measurement setup. There are two Rx coils, each with different frequency, on Tx coils. The nominal distance between Tx and Rx is 25 mm.

PMEG2015EA rectification diodes also for their low parasitic capacitance. On the other hand, the 200-kHz path employs a zero-current switching half-bridge inverter with FDD3860 MOSFETs chosen due to their low on-resistance. The input to the 200-kHz inverter is 21 V at full load. The 200-kHz receiver uses MBRA320T3G rectification diodes.

## V. MEASUREMENT

The developed measurement setup is shown in Fig. 12. For initial prototyping purposes the coils are wound around Plexiglass fixtures, which also serve to support the coils. In this setup the distance between the Tx and Rx coils are 2.5 cm. The developed

TABLE II
SYSTEM PARAMETERS

| | 6.78 MHz | 200 kHz |
|---|---|---|
| $L_F$ | 11.2 $\mu$H + 4.44 $\Omega$ | 9.6 $\mu$H + 0.116 $\Omega$ |
| $C_F$ | 47 pF | |
| $C_{\mathrm{para}}$ | 9.5 pF | |
| $C_{\mathrm{shunt}}$ | 330 pF | |
| $C_{200k}$ | 19 nF | |
| $L_{200k}$ | 23.9 $\mu$H + 8.3 $\Omega$ | 23.9 $\mu$H + 0.28 $\Omega$ |
| $L_{6.78M}$ | 1.2 $\mu$H + 0.323 $\Omega$ | |
| $L_{\mathrm{RX200}}$ | | 28.3 $\mu$H + 0.614 $\Omega$ |
| $L_{\mathrm{RX6.78}}$ | 4.4 $\mu$H + 0.958 $\Omega$ | |
| $C_{6.78M}$ | 2 nF | |
| $C_{6.78M2}$ | 440 pF | |
| $k_1$ 6.78 M system | 0.144 | |
| $k_2$, 6.78 M system | 0.144 | |
| $k_1$, 200k system | | 0.182 |
| $k_2$, 200k system | | 0.182 |
| $k_{\mathrm{TX}}$ | 0.44 | |
| Load | 10.5 V, max 0.8 A | 6 V, max 1.2 A |
| Rx coil size | 7.1 × 5.7 cm | 7.8 × 6.6 cm |

setup resembles a wireless charging pad for cellular phones, in which the Tx coil is embedded within a Tx charging pad and the receivers are placed on top of the charging pad. Charging pads are typically larger than receivers to accommodate multiple receivers, as described in each specification document [10], [11]. The advantage of the proposed Tx is that any two receivers of different frequency standards can be simultaneously charged by a single piece of Tx hardware with minimal efficiency degradation, when supporting multiband operation.

The Tx boards are powered by bench-top dc power supply, while the Rx boards have full-bridge rectifiers and power load resistors, which can withstand up to 25 W. The voltage across the dc load resistors are recorded to measure the power delivered to load. Table II summarizes the system parameters. The coupling coefficients are measured using a vector network analyzer, which produces S-parameter matrix. The same method as described in the footnote of Table I is used to extract measured coupling coefficients from S-parameter. The measured $k_{\mathrm{TX}}$ in the experimental setup is similar to the electromagnetic simulation results in Table I, while $k_1$ and $k_2$ for 200 kHz is measured to be slightly larger than simulation, since the outer dimension of the fabricated 200-kHz receiver is slightly larger than the simulation model due to fabrication tolerances.

Measured transient waveforms of the Tx inverters and Rx loads are shown in Fig. 13, during a concurrent power delivery experiment. It can be seen that the measured interference from the 200-kHz channel to the 6.78-MHz load or vice versa is very small during concurrent operation. To verify that minimal cross-talk occurs, it was observed that the 200-kHz load voltage is zero when only the 6.78-MHz Tx is operating and vice versa.

The calculated, simulated, and measured efficiencies across varying loads are presented in Figs. 14 and 15. The end-to-end efficiency of the system can be computed by multiplying the efficiencies of the Tx inverter, Tx-to-Rx coil power transfer, and the rectifier. To compute and simulate the Tx-to-Rx coil efficiency, the coils are first modeled as *RLC* circuits using parameters extracted from measurement, and the coupling coefficients between coils are extracted by the method presented in [13]. Equation (10) is then used to calculate the efficiency. The efficiencies of the Tx inverter and rectifier are difficult to simulate due to the lack of a spice model of the discrete components. Instead, inverter efficiencies are directly measured, which are 92.9% and 91.5% for the 6.78-MHz and 200-kHz inverter, respectively. The rectifier efficiency is estimated by dividing the output load voltage by the sum of forward voltage drop and output load voltage. In this manner, the 6.78-MHz and 200-kHz rectifier efficiencies are found to be 91.7% and 89.6%, respectively. It can be seen in Figs. 14 and 15 that the measured efficiency matches well with the simulated/calculated values.

Fig. 14 shows the end-to-end efficiency at 6.78 MHz operating in several different modes. The "standalone" 6.78-MHz mode is measured by disconnecting the 200-kHz Tx board from the 200-kHz Tx coil. The "concurrent" 6.78-MHz mode is measured when the 200 kHz is simultaneously operating with $L_F - C_F$ filter. At full load, the efficiency of the 6.78-MHz path in standalone mode and concurrent mode is 81.8% and 78.8%, respectively. The efficiency drops due to simultaneous operation with the 200-kHz standard are 3% and 4.2% at full and light load, respectively. In the "no filter" mode, the 6.78 MHz path is tested with the 200-kHz Tx board connected, but the $L_F - C_F$ filter is removed and the two remaining terminals are shorted by a wire. The resultant eddy current changes the effective inductance and resonant frequency of the 6.78-MHz Tx, and therefore, the resonant capacitors are adjusted to bring the resonant frequency back to 6.78 MHz. The measured efficiency in this mode is 70.4%, which is 8.4% lower than the concurrent mode with the $L_{\mathrm{F}}$–$C_{\mathrm{F}}$ filter.

Measured results of the 200-kHz path over the different operating modes are shown in Fig. 15. The "standalone" 200-kHz setup is measured by disconnecting the 6.78-MHz board, removing the $L_F - C_F$ filter, and retuning $C_{200k}$. The "concurrent" 200-kHz setup is measured, when the 6.78 MHz is simultaneously operating and the $L_F - C_F$ filter is connected. It can be seen that the efficiency of the 200-kHz mode is almost the same with or without the $L_F - C_F$ filter. The efficiency differences between "standalone" and "concurrent" are 1.3% and 4% at full and light load, respectively. The concurrent setup without the $L_F - C_F$ filter is also tested, but the efficiency is not plotted since it was measured to be the same as the "standalone" mode.

The presented measurement results are summarized in Table III for the 6.78-MHz path by describing the required Tx-coil current and resulting efficiency in the standalone mode, as well as the concurrent modes with and without the $L_F - C_F$ filter. The Tx-coil currents of the three configurations are set to deliver the same amount of power to the receiver. It can be seen that Tx current is at least 2 times larger when the eddy currents are not blocked, which matches the predictions when comparing (6) and (8) with $k_{\mathrm{TX}} = 0.44$. It can be concluded that eddy current blocking is essential to improve the efficiency and reduce

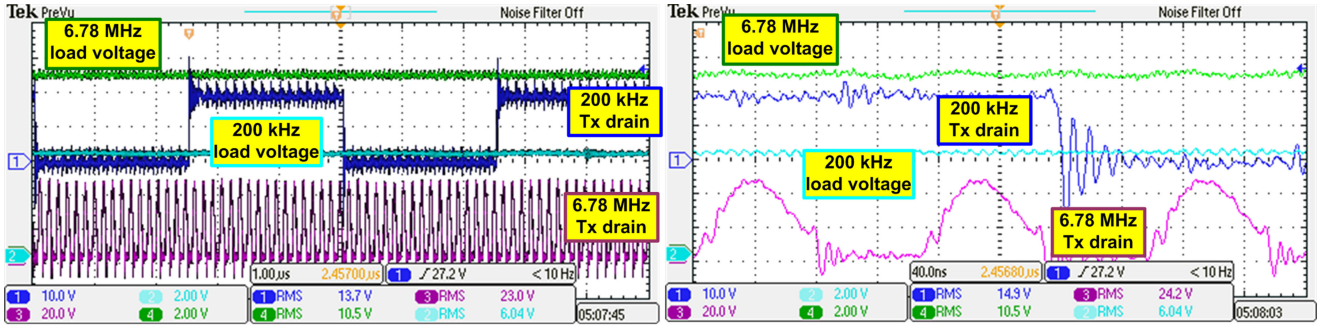


Fig. 13. Measured waveforms showing simultaneous operation. One frequency operation does not affect the other frequency mode. (a) 1 $\mu$s/div (b) 40 ns/div.

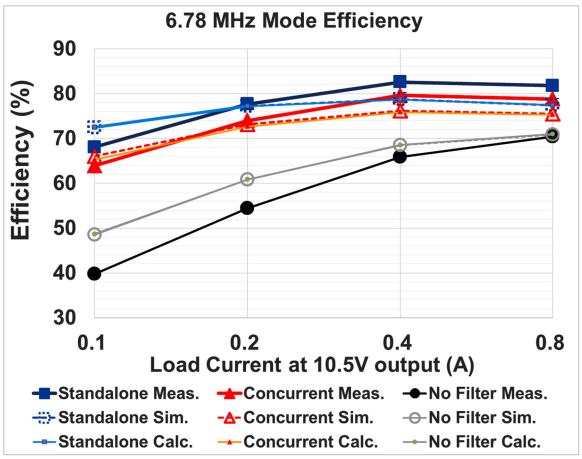


Fig. 14. 6.78-MHz efficiencies. The efficiency degradation from standalone mode due to concurrent operation is less than 4.2%. The efficiency degradations are severe, when eddy current is not blocked by $L_F - C_F$ filter.

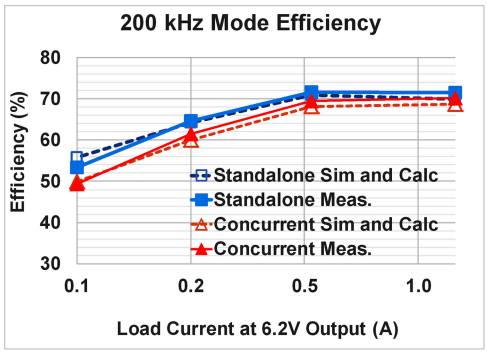


Fig. 15. 200-kHz efficiencies. The efficiency degradations due to concurrent operation are less than 4%.

the driving current requirement of a dual-mode wireless power transmitter.

The developed system is also tested for operation versus lateral misalignment. Fig. 16 summarizes the measured efficiency results. It can be seen that the concurrent operation does not significantly affect the efficiency versus lateral misalignment. It can be noted that the 6.78-MHz path can accommodate a wider lateral misalignment, since the 6.78-MHz Tx coil has a larger diameter than the 200-kHz Tx coil. As shown in Fig. 16, the power transfer efficiency is nearly constant if the misalignment is small. This is possible because under small misalignments,

TABLE III
REQUIRED TX-COIL CURRENT FOR 8.8-W RECEIVED POWER OPERATING AT 6.78 MHZ

| | Efficiency (%) | Tx-coil current RMS (A) |
|---|---|---|
| Standalone mode | 81.8 | 0.8 |
| Concurrent with *LC* filter | 78.8 | 0.75 |
| Concurrent without *LC* filter | 70.4 | 1.63 |

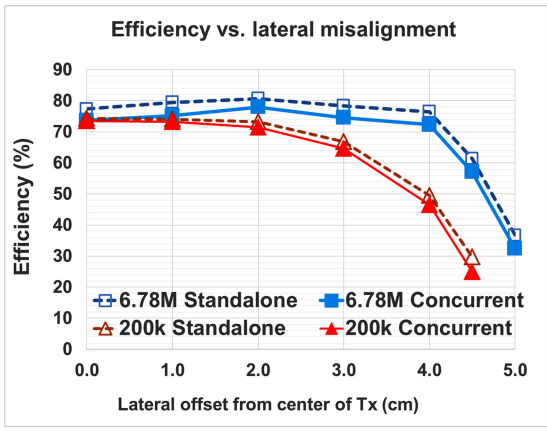


Fig. 16. Measured efficiencies versus receiver misalignment from Tx center. It can be seen that the concurrent operation does not degrade the allowable range of lateral misalignment.

$R_{\rm refl}$ is very high compared to $R_{\rm TXparasitic}$, and therefore, the efficiency equation of (2) asymptotically approaches a constant value as $R_{\rm refl}$ is increased. For example, the coupling coefficients at 200 kHz for zero-offset and 2-cm offset are simulated to be 0.163 and 0.127, respectively. However, the reflected resistances $R_{\rm refl}$ are 20 and 10 times larger than the $R_{\rm TXparasitic}$ in zero-offset and 2 cm-offset conditions, respectively. Therefore, such moderate misalignment does not significantly degrade efficiency. However, as misalignment continues to grow, for example to 4 cm, the simulated coupling coefficient at 200 kHz becomes 0.054, and thus, the $R_{\rm refl}$ is at most 2.2 times larger than $R_{\rm TXparasitic}$, resulting in an efficiency drop.

Table IV summarizes the performance of the developed system in comparison to prior art. The proposed design achieves high efficiency with concurrent delivery of power to two receivers operating at different standards-compliant frequencies.

TABLE IV
PERFORMANCE COMPARISON

| | Frequency mode | Standard | Power (W) | Efficiency (%) | Distance (mm) | Multiband capability | Multiband support location |
|---|---|---|---|---|---|---|---|
| This work | 6.78 MHz | A4WP | 9.0 | 78 | 25 | Yes | Tx side |
| | 200 kHz | WPC/PMA | 7.4 | 70.6 | | | |
| [3] | 6.78 MHz | A4WP | 5 | 48–58 | n/a | Yes | Rx side |
| | 144 kHz | WPC/PMA | 5 | 72 | | | |
| [2] | 140 kHz | WPC/PMA | 5 | 70 | 5 | No | n/a |
| [15] | 13.56 MHz | n/a | n/a | 80† | 50 | Yes | Tx and/or Rx |
| | 6.78 MHz | A4WP | n/a | 80† | | | |

† Coil-to-coil efficiency only.

## VI. CONCLUSION

This paper has demonstrated a dual-frequency wireless power transfer transmitter module that can simultaneously power two receivers operating at either 200 kHz, which is in the range of the WPC/PMA standards, or 6.78 MHz, which is supported by the A4WP standard. Achieving dual-band support, especially when the desired frequencies are an order of magnitude apart, requires careful consideration of parasitics, coil design, and eddy-current paths. While in principal, it is possible to design a single coil that operates with a dual-resonant matching network, the coil performance changes significantly over frequency, and thus, it is difficult to efficiently operate at two distinct frequencies. Alternatively, reconfiguring the coil via explicit switches suffers from significant parasitics that prevent efficient dual-band operation.

To overcome these challenges, this paper developed a two-coil, dual-band system that enables concurrent operation. Analytical expressions predicting the eddy-current losses associated with the two-coil system were presented, along with a filter design that minimizes such losses. A prototype was designed and fabricated, showing measured concurrent dual-frequency operation with minimal interference in each band. A consequence of enabling the dual-band support is the reduced efficiency compared to a design that maximizes the efficiency for a single-band only. However, the proposed design minimizes this degradation to be between 1.3% and 4.2% under various conditions through careful analysis, a novel circuit topology, and thoughtful parameter selection. Although there are two coils in the proposed Tx device, the overall coil size does not increase since the two coils are placed within each other on the same plane. The proposed coil structure and filter design allows each Tx coil to be designed for the maximum efficiency at their respective target frequencies, enabling high end-to-end efficiency even during simultaneous dual-band operation.

## APPENDIX

The parasitics of the 200-kHz Rx can also behave as an additional eddy-current loop for the 6.78-MHz signal. Fortunately, this eddy current does not contribute significant losses, since the coupling coefficient between the 6.78-MHz Tx and the 200-kHz Rx in this work (0.182) is weaker than the coupling coefficient between the 6.78-MHz Tx and the 200-kHz Tx (0.44). More importantly, the coupling coefficient between the 200-kHz Rx and the 6.78-MHz Rx is very weak (simulation predicts the coupling of 0.06), implying that the magnetic field cancelation at 6.78-MHz Rx due to the 200-kHz-Rx eddy current is minimal.

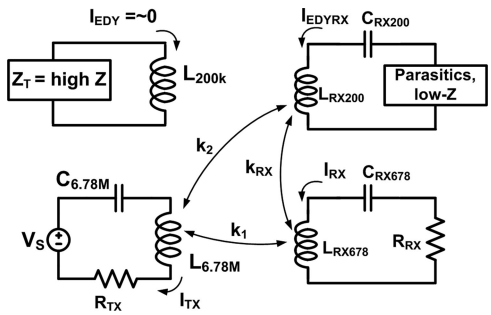


Fig. A1. Effect of the 200-kHz Rx on the 6.78-MHz operation. The 200-kHz Rx behaves as a weak eddy current loop; however, its impact is minimal due to weak $k_2$ and $k_{\mathrm{RX}}$.

Fig. A1 can be used to analyze these cross-coupling effects. The analysis is similar with Fig. 4(b) and its subsequent equations except the changes of notation. The 200-kHz Tx $L_{200k}$ is now equipped with eddy blocking $L_F - C_F$ filter, and therefore, decoupled from the system. Since the 200-kHz Rx is not equipped with an $L_F - C_F$ filter, the required Tx driving current can be evaluated using (6), which states that Tx driving current is increased by a factor of $1/(1 - (k_{\mathrm{RX}}/k_1)k_2)$ with changes in notation. Using numerical values representative of the geometries involved in this work, the Tx driving current is increased by only 8%. As a result, the impact of the 200-kHz receiver on the 6.78-MHz Tx is small. Measurement results during 6.78-MHz operation also indicate that the efficiency with and without the presence of the 200-kHz Rx is nearly the same: efficiency decreases from 78.9% to 78.8%, a degradation of only 0.1%.

## REFERENCES

[1] W. Zhong, X. Liu, and S. Hui, "A novel single-layer winding array and receiver coil structure for contactless battery charging systems with free-positioning and localized charging features," *IEEE Trans. Ind. Electron.*, vol. 58, no. 9, pp. 4136—4144, Sep. 2011.

[2] M. Galizzi, M. Caldara, V. Re, and A. Vitali, "A novel Qi-standard compliant full-bridge wireless power charger for low power devices," in *Proc. IEEE Wireless Power Transfer*, 2013, pp. 44–47.

[3] P. Riehl, A. Satyamoorthy, H. Akram, Y.-C. Yen, J.-C. Yang, B. Juan, C.-M. Lee, F.-C. Lin, V. Muratov, W. Plumb, and P. Tustin, "Wireless power systems for mobile devices supporting inductive and resonant operating modes," *IEEE Trans. Microw. Theory Tech.*, vol. 63, no. 3, pp. 780—790, Mar. 2015.

[4] Z. N. Low, R. A. Chinga, R. Tseng, and J. Lin, "Design and test of a high-power high-efficiency loosely coupled planar wireless power transfer system," *IEEE Trans. Ind. Electron.*, vol. 56, no. 5, pp. 1801–1812, May. 2009.

[5] J. Shin, S. Shin, Y. Kim, S. Ahn, S. Lee, G. Jung, S.-J. Jeon, and D.-H. Cho, "Design and implementation of shaped magnetic-resonance-based

wireless power transfer system for roadway-powered moving electric vehicles," *IEEE Trans. Ind. Electron.*, vol. 61, no. 3, pp. 1179–1192, Mar. 2014.

[6] J. Huh, S. Lee, W. Lee, G. Cho, and C. Rim, "Narrow-width inductive power transfer system for online electric vehicles," *IEEE Trans. Power Electron.*, vol. 26, no. 12, pp. 3666–3679, Dec. 2011.

[7] D. Ahn and M. Ghovanloo, "Optimal design of wireless power transmission links for millimeter-sized biomedical implants," *IEEE Trans. Biomed. Circuit Syst.*, to be published.

[8] D. Ahn and S. Hong, "Wireless power transmission with self-regulated output voltage for biomedical implant," *IEEE Trans. Ind. Electron.*, vol. 61, no. 5, pp. 2225–2235, May. 2014.

[9] X. Li, C.-Y. Tsui, and W.-H. Ki, "A 13.56 MHz wireless power transfer system with reconfigurable resonant regulating rectifier and wireless power control for implantable medical devices," *IEEE. J. Solid-State Circuits*, vol. 50, no. 4, pp. 978–989, Apr. 2015.

[10] A4WP wireless power transfer system baseline system specification, BSS Standard A4WP-S-0001 v1.2, Jan. 2014.

[11] System description wireless power transfer volume 1: Low power, Wireless Power Consortium Specification, Jun. 2013.

[12] PMA inductive wireless power and charging transmitter specification—system release 1, Standard PMA-TS-003–0 v1.00, Mar. 2014.

[13] M. Ghovanloo and S. Atluri, "A wide-band power-efficient inductive wireless link for implantable microelectronic devices using multiple carriers," *IEEE Trans. Circuits Syst.*, vol. 54, no. 10, pp. 2211–2221, Oct. 2007.

[14] Z. Pantic, K. Lee, and S. Lukic, "Multifrequency inductive power transfer," *IEEE Trans. Power Electron.*, vol. 29, no. 11, pp. 5995–6005, Nov. 2014.

[15] M.-L. Kung and K.-H. Lin, "Enhanced analysis and design method of dual-band coil module for near-field wireless power transfer systems," *IEEE Trans. Microw. Theory Tech.*, vol. 63, no. 3, pp. 821–832, Mar. 2015.

[16] M. Dionigi and M. Mongiardo, "A novel resonator for simultaneous wireless power transfer and near field magnetic communications," in *Proc. IEEE Int. Microw. Symp.*, 2012, pp. 1–3.

[17] A. Grebennikov and N. O. Sokal, *Switchmode RF Power Amplifiers*. Amsterdam, The Netherlands: Elsevier, 2007.

[18] P. P. Mercier and A. P. Chandrakasan, "Rapid wireless capacitor charging using a multi-tapped inductively-coupled secondary coil," *IEEE Trans. Circuits Syst.*, vol. 60, no. 9, pp. 2263–2272, Sep. 2013.

[19] D. Ahn and S. Hong, "Effect of coupling between multiple transmitters or multiple receivers on wireless power transfer," *IEEE Trans. Ind. Electron.*, vol. 60, no. 7, pp. 2602–2613, Jul. 2013.

[20] D. Ahn and S. Hong, "Wireless power transfer resonance coupling amplification by load-modulation switching controller," *IEEE Trans. Ind. Electron.*, vol. 62, no. 2, pp. 898–909, Feb. 2015.

**Dukju Ahn** received the B.S. degree in electrical engineering from Seoul National University, Seoul, Korea, in 2007, and the M.S. and Ph.D. degrees in electrical engineering from the Korea Advanced Institute of Science and Technology, Daejeon, Korea, in 2010 and 2012, respectively.

He is currently with Electronics and Telecommunications Research Institute, Daejeon, as a Senior Research Engineer. His research interests include wireless power transfer, near-field communication, and analog/RF integrated circuit design for biomedical and portable applications.

Dr. Ahn received the Encouragement Prize in the 17th Human-Tech Thesis Contest from Samsung Electronics in 2011.

**Patrick P. Mercier** (S'04–M'12) received the B.Sc. degree in electrical and computer engineering from the University of Alberta, Edmonton, AB, Canada, in 2006, and the S.M. and Ph.D. degrees in electrical engineering and computer science from the Massachusetts Institute of Technology (MIT), Cambridge, MA, USA, in 2008 and 2012, respectively.

He is currently an Assistant Professor in Electrical and Computer Engineering at the University of California San Diego (UCSD), where he is also the co-Director of the Center for Wearable Sensors. His research interests include the design of energy-efficient microsystems, focusing on the design of RF circuits, power converters, and sensor interfaces for miniaturized systems and biomedical applications.

Prof. Mercier received a Natural Sciences and Engineering Council of Canada (NSERC) Julie Payette fellowship in 2006, NSERC Postgraduate Scholarships in 2007 and 2009, an Intel Ph.D. Fellowship in 2009, the 2009 ISSCC Jack Kilby Award for Outstanding Student Paper at ISSCC 2010, a Graduate Teaching Award in Electrical and Computer Engineering at UCSD in 2013, the Hellman Fellowship Award in 2014, the Beckman Young Investigator Award in 2015, and the DARPA Young Faculty Award in 2015. He currently serves as an Associate Editor of the IEEE TRANSACTIONS ON BIOMEDICAL CIRCUITS AND SYSTEMS and the IEEE TRANSACTIONS ON VERY LARGE SCALE INTEGRATION, and is a co-editor of Ultra-Low-Power Short-Range Radios (Springer, 2015).